






# Shadow and accretion disk images of the rotation loop quantum black bounce\*

Ke-Jian He (何柯健)<sup>1</sup>  Huan Ye (叶欢)<sup>2</sup>  Xiao-Xiong Zeng (曾晓雄)<sup>3</sup>  Li-Fang Li (李丽仿)<sup>4†</sup> 

Peng Xu (徐鹏)<sup>4,5,6</sup> 

<sup>1</sup>Department of Mechanics, Chongqing Jiaotong University, Chongqing 400000, China

<sup>2</sup>School of Material Science and Engineering, Chongqing Jiaotong University, Chongqing, 400074, China

<sup>3</sup>College of Physics and Electronic Engineering, Chongqing Normal University, Chongqing 401331, China

<sup>4</sup>Center for Gravitational Wave Experiment, National Microgravity Laboratory, Institute of Mechanics, Chinese Academy of Sciences, Beijing 100190, China

<sup>5</sup>Lanzhou Center of Theoretical Physics, Lanzhou University, Lanzhou 730000, China

<sup>6</sup>Taiji Laboratory for Gravitational Wave Universe (Beijing/Hanzhou), University of Chinese Academy of Sciences, Beijing 100049, China

**Abstract:** In this study, we investigate the shadow and observational image of the Kerr-like Loop Quantum Gravity (LQG) inspired black bounce with the help of the celestial light and thin disk sources by employing the backward ray-tracing method. The results indicate that both the LQG parameter  $\alpha$  and rotation parameter  $a$  contribute to a reduction in the shadow size. However, the influence of  $a$  is predominant, whereas that of  $\alpha$  is supplementary. For the accretion disk model, we extend its inner edge to the black hole's event horizon, and the motion of particles is different in the regions inside and outside the innermost stable circular orbit. We find that the correlation parameters  $(a, \alpha)$ , along with the observer's inclination angle, affect the image's asymmetry and the distortion of the inner shadow. As the inclination increases, the direct and lensed images diverge, creating a structure resembling a hat. Moreover, we investigate the redshift distribution of the direct lensed images of the accretion disk under different parameters and observation angles. The results show that the redshift distribution and observed intensity are evidently related to the behavior of accretion flow. These results may provide a potential approach for limiting black hole parameters, detecting quantum gravity effects, and distinguishing the LQG black hole from other black hole models.

**Keywords:** black hole shadow, black hole image, loop quantum cosmology

**DOI:** 10.1088/1674-1137/adf4a2

**CSTR:** 32044.14.ChinesePhysicsC.49125103

## I. INTRODUCTION

In recent decades, significant advancements have been achieved in the field of black hole research, particularly concerning the investigation of their shadows and observed images. Black hole shadows, which are caused by the inability of light to escape from a black hole's event horizon, have transitioned from theoretical speculation to empirical validation, marking a pivotal moment in physical and astronomical research. Technological advancements in radio astronomy and space telescopes have enabled astronomers to search for these elusive shadows. In 2019, the Event Horizon Telescope (EHT) collaboration announced the first direct image of a black hole shadow, which was captured from the supermassive black hole at the center of the M87 galaxy [1–6]. This groundbreaking achievement was subsequently complemented by the imaging of another black hole shadow, originating

from the supermassive black hole at the center of our Milky Way, Sagittarius A\*, in 2022 [7–12]. These images not only confirmed the predictions of general relativity but also created new avenues for testing and refining our understanding of gravity and cosmology.

For a long time, black hole shadows and their observable phenomena have been pivotal topics of research. Illustratively, the shadow of a Schwarzschild black hole appears as a black disk regardless of the viewing angle [13]. For a Kerr black hole, an observer positioned in the equatorial plane would observe its shadow changing shape with the rotation parameter. As the rotation parameter increases, the black disk gradually evolves into a D-shape [14, 15]. Subsequently, extensive investigations were conducted on the shadows of the rotating EMDA black hole [16], non-commutative black hole [17], phantom black hole [18], Konoplya-Zhidenko rotating non-Kerr black hole [19], and Finslerian-Schwarzschild

Received 2 April 2025; Accepted 8 July 2025; Published online 9 July 2025

\* Supported by the National Natural Science Foundation of China (12375043)

† E-mail: lilifang@imech.ac.cn (Corresponding author)

©2025 Chinese Physical Society and the Institute of High Energy Physics of the Chinese Academy of Sciences and the Institute of Modern Physics of the Chinese Academy of Sciences and IOP Publishing Ltd. All rights, including for text and data mining, AI training, and similar technologies, are reserved.

black hole [20]; cusp-like structures; and other intriguing effects [21–33]. Furthermore, significant advancements have been achieved in the study of black hole shadows and photon rings through the application of wave optics within the holographic framework [34–40].

The visual representation of a black hole is intrinsically linked to the properties and behavior of the accreting material surrounding it. By considering the spherically symmetric accretion model, Narayan *et al.* studied the optical appearance of Schwarzschild black holes [41]. Building on this foundation, Wald *et al.* demonstrated that, when a Schwarzschild black hole is encircled by an accretion disk, an observer positioned at the north pole would observe the black hole's shadow as a dark disk surrounded by a distinctive bright ring. This luminous ring comprises direct emissions, a lensing ring, and a photon ring [42]. Subsequently, this phenomenon was extended to a broader range of static spherically symmetric black holes, including those containing matter fields and modified gravities, as well as wormhole spacetime [43–60]. Naturally, the shadow of a rotating black hole surrounded by an accretion disk has also been studied. Hou *et al.* analyzed the effects of rotation, magnetic field, and observer angle on multistage images of a rotating Kerr-Melvin black hole, discussing the accretion disk model in depth [61]. Subsequently, the observed features of rotating black holes illuminated by accretion disks were further generalized in other modified gravitational backgrounds [57, 62–66].

Furthermore, Loop Quantum Gravity (LQG) represents one of the most promising theories in quantifying gravity [67–72] and aims to bridge the gap between Einstein's theory of general relativity and quantum mechanics [73–74]. Over the decades, LQG has evolved into a well-defined and mathematically rigorous theory. Unlike other attempts to quantize gravity using perturbative methods, LQG adopts a non-perturbative and background-independent approach [75–78]. One of the significant achievements of LQG is the physical spectra of geometrical quantities such as area and volume, which yields quantitative predictions on Planck-scale physics. Additionally, LQG has derived the Bekenstein-Hawking black hole entropy formula and provided an intriguing physical picture of the microstructure of quantum physical space [79–83]. This discreteness emerges naturally from quantum theory and offers a mathematically well-defined realization of Wheeler's intuition of a spacetime foam [84–86]. More importantly, the solutions of a rotating LQG black hole derived within this gravitational theory exhibit a non-singular geometry that we expect owing to the existence of the transition surface. This solution transcends the specifics of the seed metric used, thereby effectively capturing some universal characteristics of rotating LQG black holes. Muniz *et al.* investigated a static and stationary black bounce geometry in-

spired by LQG, focusing on the effects of LQG correction terms and regularization parameters on its properties. In the Kerr-like LQG-inspired black bounce spacetime, they found that increasing the LQG parameter causes the ergospheres, as well as the shadow shape, to become smaller [87]. However, the question on whether this Kerr-like LQG-inspired black bounce is observable is unsettled in astronomy. Given the advancements in black hole imaging, the shadow, inner shadow, celestial source images, and thin disk images of the Kerr-like LQG-inspired black bounce are important to study using the thin disk accretion model. In this study, we investigate the observable astronomical effects of the Kerr-like LQG-inspired black bounce, thereby providing a viable reference framework for the analysis of quantum effects of black holes.

The remainder of this paper is structured as follows. In Section II, we briefly review black holes in LQG and the characteristics of the Kerr-like LQG-inspired black bounce. The motion behavior of particles in Kerr-like LQG-inspired black bounce spacetime is further discussed. In Section III, we discuss the shadow of the Kerr-like LQG-inspired black bounce and examine the influence of the change of relevant parameters on the shape and size of the shadow. In Section IV, the images of black holes with the celestial light source are presented. Section V discusses the images illuminated by the thin accretion disk. Finally in the last section, we present a brief conclusion and discussion.

## II. REVIEW OF THE LOOP QUANTUM BLACK BOUNCE

Following the successful development of the Loop Quantum Cosmology model (LQC), a novel black hole solution has been discovered through the application of LQG quantization techniques to the spherically symmetric solution [88–89]. Within the framework of the Oppenheimer-Snyder (OS) collapse model, particularly in the context of spherically symmetric spacetime, an effective Hamiltonian and its corresponding metric are formulated to characterize the vacuum exterior solution. Thus, the line element has the form given by [88]

$$ds^2 = N(r)dt^2 - N(r)^{-1}dr^2 - r^2d\Omega^2, \quad (1)$$

and

$$N(r) = 1 - \frac{2M}{r} + \frac{\alpha^2 M^2}{r^4}. \quad (2)$$

Here,  $d\Omega^2 = d\theta^2 + \sin^2\theta d\phi^2$  is the line element on a unit sphere, and the mass of the black hole is denoted by  $M$ . In addition, the specific form of the term  $\alpha^2$  is

$$\alpha^2 = 16\sqrt{3}\pi\gamma^3 l_p^2, \quad (3)$$

where  $l_p$  denotes the Planck length, and  $\gamma$  represents the Barbero-Immirzi parameter. The horizons can be determined by imposing  $N(r) = 0$ , and we find two horizons, namely, the inner and outer horizons, which are

$$r_{\text{inner}} = \left(\frac{\alpha^2 M}{2}\right)^{1/3} + \frac{1}{6} \left(\frac{\alpha^4}{4M}\right)^{1/3},$$

$$r_{\text{outer}} = 2M - \left(\frac{\alpha^2}{8M}\right)^{1/3}. \quad (4)$$

Note that the domain of radial coordinates is constrained by establishing a minimum radius from the lower limit, thereby addressing the singularity issue. This minimum radius is defined as

$$r > r_b = (\alpha^2 M/2)^{1/3}. \quad (5)$$

This lower bound is consistent with the fact that the radial coordinate of the dust surface ranges over  $[r_b, \infty)$  [89]. The condition  $r > r_b$  in this metric fundamentally reflects how quantum gravitational effects establish a minimal characteristic scale  $r_b$  within the black hole. This critical scale  $r_b$  serves as both the physical boundary for the dusty part of the spacetime and the validity threshold for semi-classical theory. Below this scale ( $r < r_b$ ), quantum correction terms become dominant and require a non-perturbative quantum gravity description. In the context of (1), it can be naturally extended to the region where  $r \rightarrow 0$ , which is characterized by a singularity. This outcome is not expected, and a robust analytical approach is required to address the singularity issue without artificially constraining the domain of  $r$ . A commendable approach is the Simpson-Visser prescription [90], which fundamentally involves substituting  $r \rightarrow \sqrt{r^2 + \tilde{a}^2}$ , where  $\tilde{a}$  serves as a regularization parameter. By applying the Simpson-Visser prescription  $r \rightarrow \sqrt{r^2 + r_b^2}$ , we can obtain the line element of the Loop Quantum Black Bounce (LQBB), which is [87]

$$ds^2 = \left[1 - \frac{2M}{\sqrt{r^2 + r_b^2}} + \frac{\alpha^2 M^2}{(r^2 + r_b^2)^2}\right] dt^2$$

$$- \left[1 - \frac{2M}{\sqrt{r^2 + r_b^2}} + \frac{\alpha^2 M^2}{(r^2 + r_b^2)^2}\right]^{-1} dr^2$$

$$- (r^2 + r_b^2) d\Omega^2, \quad (6)$$

In practice, the parameter  $r_b$  can be considered a free parameter. In certain scenarios, the bounce radius can be expressed as a function of  $\alpha$  according to Eq. (5), without any loss of generality. From the Ricci scalar, denoted as

$$R = \frac{6\alpha^2 M^2 r^2 + 2r_b^2 (r^2 + r_b^2)^{3/2} (\sqrt{r_b^2 + r^2} - 3M)}{(r_b^4 + r^2)^4}, \quad (7)$$

we observe that the black bounce exhibits regularity throughout the entire domain of  $r$ . The relevant characteristics of the LQBB have been well studied; see [87]. The Newman-Janis algorithm (NJA) is widely recognized as the standard method for deriving the rotating black hole metric from the static spherically symmetric solution [91–92]. For instance, the studies reported in Refs. [93–94] used this method to construct the first observationally viable rotating black hole in LQG, yielding a singularity-free solution that matches Kerr asymptotically and enables direct tests of LQG through black hole shadows. The universal structure of the model, covering both horizonless and horizon-bearing cases, bridges a crucial gap between quantum gravity theory and astrophysical observations. In this paper, the rotating solution of the LQG-inspired black bounce we used is expressed as [87, 93, 94]

$$ds^2 = \frac{\Psi}{\rho^2} \left\{ \frac{\Delta}{\rho^2} (dt - a \sin^2 \theta d\phi)^2 - \frac{\rho^2}{\Delta} dr^2 - \rho^2 d\theta^2 \right.$$

$$\left. - \frac{\sin^2 \theta}{\rho^2} [adt - (r^2 + r_b^2 + a^2) d\phi]^2 \right\}, \quad (8)$$

where

$$\Delta = (r^2 + r_b^2) \left[ 1 - \frac{2M}{\sqrt{r^2 + r_b^2}} + \frac{\alpha^2 M^2}{(r^2 + r_b^2)^2} \right] + a^2, \quad (9)$$

and

$$\rho^2 = r^2 + r_b^2 + a^2 \cos^2 \theta. \quad (10)$$

Here, the rotation parameter is represented by  $a$ , and when the LQG parameter  $\alpha = 0$ , the solution reduces to the Kerr spacetime. In addition to satisfying Einstein's field equations, the function  $\Psi = \Psi(r, \theta, a)$  must fulfill the condition  $G_{r\theta} = 0$ . Consequently, in this solution,  $\Psi$  is expressed as  $\rho^2 = \Psi$ , and the horizons are determined by the condition  $\Delta = 0$ . Note that the rotating LQBB spacetime exhibits a singularity when  $r^2 + r_b^2 + a^2 \cos^2 \theta = 0$ . However, given the condition that  $r_b \neq 0$ , this particular configuration ensures that the singularity is not present in this spacetime.

### III. SHADOW OF THE KERR-LIKE LQG-INSPIRED BLACK BOUNCE

In the background of rotating LQBB spacetime, to investigate the shadow cast by the black hole, we must analyze the behavior of photons within this spacetime. To study photon trajectories effectively, we must first examine their geodesic structure, which is described by the

Hamilton-Jacobi equation

$$\frac{\partial \mathcal{I}}{\partial \lambda} = -\frac{1}{2} g^{\mu\nu} \frac{\partial \mathcal{I}}{\partial x^\mu} \frac{\partial \mathcal{I}}{\partial x^\nu}, \quad (11)$$

where  $\lambda$  is the affine parameter of the null geodesic, and  $\mathcal{I}$  denotes the Jacobi action of the photon.  $\mathcal{I}$  can be separated in the following form:

$$\mathcal{I} = \frac{1}{2} u^2 \lambda - \vec{E} t + \vec{L} \phi + \mathcal{I}_r(r) + \mathcal{I}_\theta(\theta). \quad (12)$$

In the above, the term  $u$  is the mass of the particle moving in the black hole spacetime; for a photon,  $u = 0$ . In addition,  $\vec{E} = -p_t$  and  $\vec{L} = p_\theta$  represent the conserved energy and conserved angular momentum of the photon along the rotation axis, respectively. The functions  $\mathcal{I}_r(r)$  and  $\mathcal{I}_\theta(\theta)$  depend solely on  $r$  and  $\theta$ , respectively. By substituting the Jacobi action (12) into the Hamilton-Jacobi equation (11), we can obtain the following four equations of motion for the evolution of the photon [87]:

$$\Sigma \frac{dt}{d\lambda} = \frac{1}{\Delta} (\vec{E}(r^2 + a^2) - a\vec{L}) (r^2 + a^2) - a(a\vec{E} \sin^2 \theta - \vec{L}), \quad (13)$$

$$\Sigma \frac{d\phi}{d\lambda} = \frac{a}{\Delta} (\vec{E}(r^2 + a^2) - a\vec{L}) - \frac{1}{\sin^2 \theta} (a\vec{E} \sin^2 \theta - \vec{L}), \quad (14)$$

$$\Sigma \frac{dr}{d\lambda} = \pm \sqrt{\mathbf{R}(r)}, \quad (15)$$

$$\Sigma \frac{d\theta}{d\lambda} = \pm \sqrt{\Theta(\theta)}. \quad (16)$$

and

$$\mathbf{R}(r) = (\chi(r)\vec{E} - a\vec{L})^2 - \Delta(r)(Q + (\vec{L} - a\vec{E})^2), \quad (17)$$

$$\Theta(\theta) = Q + a^2 \vec{E}^2 \cos^2 \theta - \vec{L}^2 \cot^2 \theta. \quad (18)$$

where the quantity  $Q$  is the generalized Carter constant, and  $\chi(r) = (r^2 + a^2)$ . The unstable spherical orbit of the black hole is the key condition for determining the shadow boundary, and it should follow the condition

$$\dot{r} = 0, \quad \ddot{r} = 0. \quad (19)$$

By introducing two impact parameters, *i.e.*,  $\varsigma = \vec{L}/\vec{E}$  and  $\zeta = Q/\vec{E}^2$ , Eq. (19) can be expressed as

$$(\chi(r_{ph}) - a\varsigma)^2 - \Delta(r_{ph})(\zeta + (\varsigma - a)^2) = 0, \quad (20)$$

$$2\chi'(r_{ph})(\chi(r_{ph}) - a\varsigma) - \Delta'(r_{ph})(\zeta + (\varsigma - a)^2) = 0. \quad (21)$$

Here,  $r = r_{ph}$  is the radius of the unstable photon orbit. By solving above equations, we can obtain

$$\varsigma = \frac{\chi(r_{ph})\Delta'(r_{ph}) - 2\Delta(r_{ph})\chi'(r_{ph})}{a\Delta'(r_{ph})}, \quad (22)$$

and

$$\zeta = \frac{4a^2\chi'^2(r_{ph})\Delta(r_{ph}) - (\chi(r_{ph}) - a^2)\Delta'(r_{ph}) - 2\chi'(r_{ph})\Delta^2(r_{ph})}{a^2\Delta'^2(r_{ph})}. \quad (23)$$

An observer at infinity ( $r_{\text{obs}} \rightarrow \infty$ ) can be defined as a zero angular momentum observer (ZAMO) at coordinates ( $t_{\text{obs}} = 0, r_{\text{obs}}, \theta_{\text{obs}}, \phi_{\text{obs}} = 0$ ) by considering the symmetry in the directions of  $t$  and  $\phi$ . Hence, a locally orthonormal frame can be established within the vicinity of the observer, which is

$$e_0 = \left( \sqrt{\frac{-g_{\phi\phi}}{g_{tt}g_{\phi\phi} - g_{t\phi}^2}}, 0, 0, -\frac{g_{t\phi}}{g_{\phi\phi}} \sqrt{\frac{-g_{\phi\phi}}{g_{tt}g_{\phi\phi} - g_{t\phi}^2}} \right), \quad (24)$$

$$e_1 = \left( 0, -\frac{1}{\sqrt{g_{rr}}}, 0, 0 \right), \quad (25)$$

$$e_2 = \left( 0, 0, \frac{1}{\sqrt{g_{\theta\theta}}}, 0 \right), \quad (26)$$

$$e_3 = \left( 0, 0, 0, -\frac{1}{\sqrt{g_{\phi\phi}}} \right). \quad (27)$$

In this setup,  $e_0$  corresponds to the timelike vector representing the observer's four-velocity. Meanwhile,  $e_1$  designates the spatial orientation toward the black hole's core, and  $g_{\mu\nu}$  describes the black hole's background metric. This particular framework is not exclusive; different reference frames can be converted into one another via Lorentz transformations. An efficient technique for visualizing the shadow's outline on the observer's sky plane involves utilizing a pinhole camera for perspective projection, as outlined in [19]. This model is straightforward and effectively represents the actual imaging principles. However, it is constrained by a limited field of view. Consequently, we will utilize the imaging approach outlined in [95], commonly known as the fisheye lens cam-

era model. To establish the position of the photon relative to the observer, we employ celestial coordinates  $(\gamma, \xi)$ . For a light ray  $\mathcal{F}(\tau) = \{t(\tau), r(\tau), \theta(\tau), \varphi(\tau)\}$ , the tangent vector associated with this curve is defined by

$$\begin{aligned} \dot{\mathcal{F}} &= i\partial_t + \dot{r}\partial_r + \dot{\theta}\partial_\theta + \dot{\varphi}\partial_\varphi \\ &= |\overrightarrow{OP}|(-\varrho e_0 + \cos\gamma e_1 + \sin\xi \cos\gamma e_2 + \sin\gamma \sin\xi e_3). \end{aligned} \quad (28)$$

Notably, the negative sign ensures that the tangent vector is oriented towards the past, and the dot denotes the partial derivative with respect to the affine parameter  $\lambda$ . Because the path of the photon does not depend on its energy, the energy of the photon is incorporated into the camera's coordinate system and normalized to 1, that is

$$E_{\text{camera}} = 1 = |\overrightarrow{OP}| \cdot \varrho = -\frac{E}{\sqrt{g_{tt}}} |_{(r_{\text{obs}}, \theta_{\text{obs}})}. \quad (29)$$

Moreover, within the ZAMO frame, the four-momentum of photons can be represented as  $p_{(\mu)} = p_\nu e_{(\mu)}^\nu$ , and the components  $e_{(\mu)}^\nu$  are detailed in Eqs. (24)–(27). Based on the relationship between the photon four-momentum and celestial coordinates described in [102], we can obtain

$$\cos\gamma = \frac{p^{(1)}}{p^{(0)}}, \quad \tan\xi = \frac{p^{(3)}}{p^{(2)}}. \quad (30)$$

To further establish the relationship between celestial coordinates  $(\gamma, \xi)$  and Cartesian coordinates  $(x, y)$  on the screen, we derive

$$\begin{aligned} x(r_{ph}) &= -2 \tan\left[\frac{\gamma(r_{ph})}{2}\right] \sin[\xi(r_{ph})], \\ y(r_{ph}) &= -2 \tan\left[\frac{\gamma(r_{ph})}{2}\right] \cos[\xi(r_{ph})]. \end{aligned} \quad (31)$$

Thus, the boundary of the shadow can be illustrated on the observation screen. More significantly, we explore the effects of the LQG parameter  $\alpha$  and rotation parameter  $a$  on the appearance of the shadow of a rotating LQBB; see Fig. 1. We set  $\alpha = 0.1$  and  $\theta = 65^\circ$  while varying  $a$  as  $a = 0.2, 0.4, 0.7, 0.99$ . The size of the shadow on the  $y$ -axis remains constant with different  $a$  values, but the shadow contours gradually deform when  $a$  increases. At a smaller  $a$  value ( $a = 0.3$ ), the shadow contours retain a distorted circular shape, whereas at a larger  $a$  value ( $a = 0.99$ ), the shadow contours are fully presented in a D-shape. Subsequently,  $\alpha$  decreases the shadow radius when we fix the value of  $a = 0.3$  for  $\theta_{\text{obs}} = 65^\circ$ . From Fig. 1(b), we clearly observe that the shadow radius decreases with increasing  $\alpha$ . In addition, an interesting phenomenon is shown in Fig. 1(c). When both the observed inclination and rotation parameters are large ( $a = 0.99, \theta_{\text{obs}} = 65^\circ$ ), as  $\alpha$  increases, the shadow's outline exhibits an extreme D-shape with a significant overlap on the right side, whereas its size tends to contract on the left side of the  $x$ -axis. This change could become a relevant discriminator for quantum gravity signatures.

#### IV. IMAGE OF BLACK HOLE ILLUMINATED BY A CELESTIAL LIGHT SOURCE

To better observe the image of the rotating black hole, we employ the backward ray-tracing method in the framework of a celestial light source. As we know, the backward ray-tracing method enables us to trace fewer light rays, without considering those that are emitted from the light source but do not reach to the observer, which provides a convenient way to study black hole images.

To fully specify our imaging setup, we now supplement the definition of the field of view. The field of view  $\phi_v$  determines the visible range of the camera. For computational convenience, we take  $\phi_v/2$  along both the  $x$  and  $y$  directions in the Cartesian coordinates, thereby defining a square screen with side length:

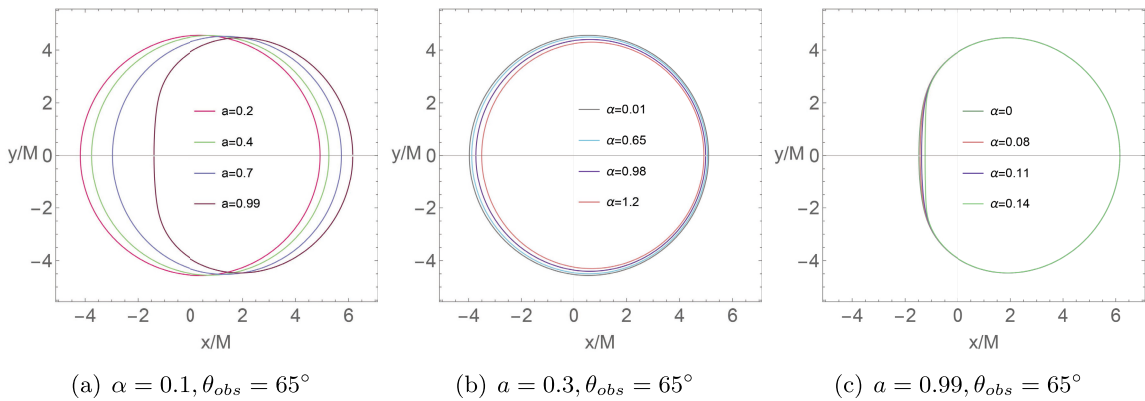


**Fig. 1.** (color online) Shadow contours of a rotating loop quantum black bounce for varying parameters  $(\alpha, a)$ , with  $\theta_{\text{obs}} = 65^\circ$  and  $M = 1$ .



$$L = 2|\vec{OP}| \tan \frac{\phi_v}{2}, \quad (32)$$

where  $\vec{OP}$  denotes the photon's three-momentum. The image plane is discretized into  $n \times n$  pixels, each with an edge length

$$l = \frac{L}{n} = \frac{2}{n} |\vec{OP}| \tan \frac{\phi_v}{2}, \quad (33)$$

and each pixel center is labeled by coordinates  $(i, j)$ , where the bottom-left pixel is indexed as  $(1, 1)$  and the top-right as  $(n, n)$ . The indices  $i$  and  $j$  range from 1 to  $n$ . The relationship between the Cartesian coordinates  $(x, y)$  and pixel index  $(i, j)$  is given by

$$x = l \left( i - \frac{n+1}{2} \right), \quad y = l \left( j - \frac{n+1}{2} \right). \quad (34)$$

By comparing Eqs. (31) and (34), the correspondence between the pixel index  $(i, j)$  and celestial coordinates  $(\gamma, \xi)$  can be expressed as

$$\begin{aligned} \tan \frac{\gamma}{2} &= \frac{1}{n} \tan \left( \frac{\phi_v}{2} \right) \sqrt{\left( i - \frac{n+1}{2} \right)^2 + \left( j - \frac{n+1}{2} \right)^2}, \\ \tan \xi &= \frac{2j - (n+1)}{2i - (n+1)}. \end{aligned} \quad (35)$$

Figure 2 shows a fisheye camera field of view with  $n \times n$  pixels.

We consider the black hole to be located at the center of the celestial sphere, with its size being significantly smaller than both the sphere itself and the distance between the observer and origin. The rotational axis of the black hole is aligned toward the celestial north pole, whereas the observer is positioned within the equatorial plane of the sphere. To enhance the clarity of light trajectories in different regions, we can divide the celestial sphere into four quadrants, each designated by a distinct color. The pink quadrant is defined by the angular ranges  $0 \leq \theta \leq \pi/2$  and  $0 \leq \phi \leq \pi$ . The blue quadrant corresponds to  $0 \leq \theta \leq \pi/2$  and  $\pi \leq \phi \leq 2\pi$ . The green quadrant is characterized by  $\pi/2 \leq \theta \leq \pi$  and  $0 \leq \phi \leq \pi$ . Finally, the orange quadrant is specified by  $\pi/2 \leq \theta \leq \pi$  and  $\pi \leq \phi \leq 2\pi$ .

With the backward ray-tracing method, the color of the light ray can be identified when the position of such a light ray reaching the celestial sphere is determined. By employing the fisheye camera model, we successfully obtain the shadow region of the black hole on the screen for a celestial sphere light source in the first row of Fig. 3, where  $r_{\text{obs}} = 120$ ,  $\theta_{\text{obs}} = 65^\circ$ , and the field of view is  $\phi_v =$

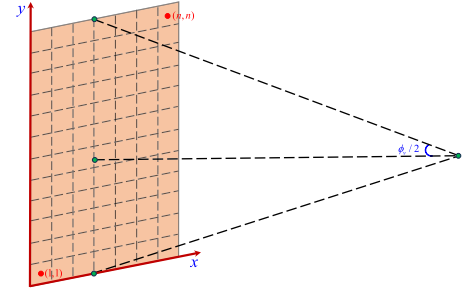


**Fig. 2.** (color online) Fisheye camera field of view with  $n \times n$  pixels.

$30^\circ$ . From the first row of Fig. 3, we observe that an increase in  $\alpha$  results in a notable bending of the light surrounding the black hole. However, this effect is comparatively minor relative to the optical distortion caused by variations in the black hole's spin. As  $a$  increases, the color image near the shadow contour<sup>1)</sup> region distorts, indicating a drag effect due to rotation in the LQBB spacetime. To more clearly observe the changes in the shadow, we can reduce the field of view value while keeping the other parameters unchanged, as illustrated in the second row of Fig. 3. As  $a$  increases, the shape of the shadow contour region gradually evolves into a D-shape, which is consistent with our previous discussion. Concurrently, the extent of the shadow contour region will also diminish as  $\alpha$  increases. In particular, as a consequence of gravitational lensing, an Einstein ring will appear exterior to the shadow, corresponding to the white ring depicted in Fig. 3.

## V. THIN ACCRETION DISK MODEL AND ITS IMAGE

### A. Setup of the thin accretion disk model

Because the millimeter-wave images of supermassive black holes are primarily influenced by their surrounding accretion disks, this section employs an accretion disk model as the light source to investigate the imaging characteristics of the LQBB. The accretion disk is modeled as a freely orbiting, electrically neutral plasma along an equatorial timelike geodesic, forming a disk that is both optically and geometrically thin. We assume that the accretion disk originates at the event horizon of the LQBB spacetime, denoted as  $r_h$ , and extends outward to a distant location, with the final radius set at  $r_f = 1000$ . The observer  $r_{\text{obs}}$  is located in the region  $r_h \ll r_{\text{obs}} < r_f$ . To obtain the black hole image in this thin disk, first we must determine the position of the inner stable circular orbit (ISCO). The radius of the ISCO can be determined by solving the following equations:

<sup>1)</sup> In this work, the black hole shadow refers to the region enclosed by the critical curve, while the subsequently discussed "inner shadow" is fundamentally defined as the directional emission from the event horizon [96].

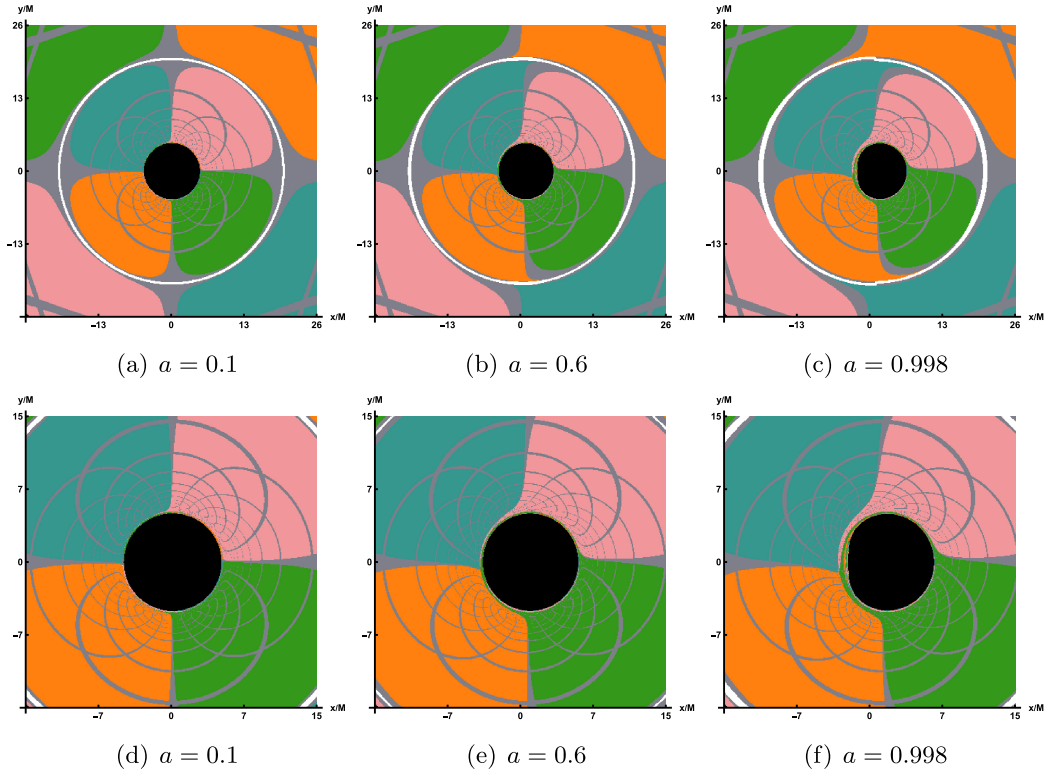


**Fig. 3.** Shadow of the LQBB under several representative parameters, obtained using the numerical ray-tracing method, where  $\alpha = 0.01$ ,  $r_{\text{obs}} = 100$ , and  $\theta_{\text{obs}} = 75^\circ$ . For the first row, the field of view is  $\phi_v = 30^\circ$ , and for the second row,  $\phi_v = 17^\circ$ .

$$V_{\text{eff}}(r, \mathcal{E}, \mathcal{L}) = 0, \quad (36)$$

$$\partial_r V_{\text{eff}}(r, \mathcal{E}, \mathcal{L}) = 0, \quad (37)$$

$$\partial_r^2 V_{\text{eff}}(r, \mathcal{E}, \mathcal{L}) = 0. \quad (38)$$

where  $V_{\text{eff}}$  is the effective potential function, and we have

$$V_{\text{eff}}(r, \mathcal{E}, \mathcal{L}) = (1 + g^{tt} \mathcal{E}^2 + g^{\phi\phi} \mathcal{L}^2 - 2g^{t\phi} \mathcal{E} \mathcal{L})|_{\theta=\frac{\pi}{2}}. \quad (39)$$

In this context,  $\mathcal{E}$  and  $\mathcal{L}$  represent the conserved quantities corresponding to the specific energy and specific angular momentum of a massive neutral particle, respectively. Their explicit forms are given by

$$\mathcal{E} = -\frac{g_{tt} + g_{t\phi} \Omega_F}{\sqrt{-g_{tt} - 2g_{t\phi} \Omega_F - g_{\phi\phi} \Omega_F^2}}, \quad (40)$$

$$\mathcal{L} = \frac{g_{t\phi} + g_{\phi\phi} \Omega_F}{\sqrt{-g_{tt} - 2g_{t\phi} \Omega_F - g_{\phi\phi} \Omega_F^2}}, \quad (41)$$

with

$$\Omega_F = \frac{d\phi}{dt} = \frac{\partial_r g_{t\phi} + \sqrt{\partial_r^2 g_{t\phi} - \partial_r g_{tt} \partial_r g_{\phi\phi}}}{\partial_r g_{\phi\phi}}, \quad (42)$$

At the position of the ISCO, we denote the conserved quantities as  $\mathcal{E}_{\text{ISCO}}$  and  $\mathcal{L}_{\text{ISCO}}$ . In the regions interior and exterior to the ISCO, accreting materials demonstrate distinct dynamical behaviors [61]. In other words, the motion of accretion flows inside and outside the ISCO differs, necessitating the separate determination of their four-velocities in each region. First, outside the ISCO, *i.e.*,  $r_{\text{ISCO}} < r$ , the accretion flows in the accretion disk moves along nearly circular orbits. The four-velocity is given by

$$u_{\text{out}}^\mu = \sqrt{\frac{1}{-g_{tt} - 2g_{t\phi} \Omega_F - g_{\phi\phi} \Omega_F^2}} (1, 0, 0, \Omega_F) \Big|_{\theta=\pi/2}. \quad (43)$$

Subsequently, within the ISCO  $r_h < r < r_{\text{ISCO}}$ , the accretion flows descend from the ISCO to the event on a critical plunging orbits while maintaining the same conserved quantities associated with the ISCO. For convenience, the conserved quantities  $\mathcal{E}_{\text{ISCO}}$  and  $\mathcal{L}_{\text{ISCO}}$  are equal to the values at the ISCO. Here, the four-velocity is given by

$$u_{\text{in}}^t = (-g^{tt}\mathcal{E}_{\text{ISCO}} + g^{t\phi}\mathcal{L}_{\text{ISCO}})|_{\theta=\pi/2}, \quad (44)$$

$$u_{\text{in}}^\phi = (-g^{t\phi}\mathcal{E}_{\text{ISCO}} + g^{\phi\phi}\mathcal{L}_{\text{ISCO}})|_{\theta=\pi/2}, \quad (45)$$

$$u_{\text{in}}^r = -\sqrt{-\frac{-g_{tt}u_{\text{in}}^t u_{\text{in}}^t + 2g_{t\phi}u_{\text{in}}^t u_{\text{in}}^\phi + g_{\phi\phi}u_{\text{in}}^\phi u_{\text{in}}^\phi + 1}{g_{rr}}}|_{\theta=\pi/2}, \quad (46)$$

$$u_{\text{in}}^\theta = 0. \quad (47)$$

Note that the negative sign before the square root expresses the direction towards the event horizon. We subsequently trace the light rays backward, originating from the observer's position. These rays may intersect the accretion disk in the equatorial plane once ( $n=1$ ), twice ( $n=2$ ), or multiple times ( $n>2$ ). Each intersection point contributes to the observed luminosity, and the radial position at each intersection is denoted as  $r_n(x, y)|_{n=1,2,3,\dots,N}$ .  $r_n(x, y)$  denotes the  $n^{\text{th}}$  image displayed on the screen. Specifically, when  $n=1$ , the image is referred to as the direct image, whereas when  $n=2$ , it is called the lensed image. To further elaborate, when we do not consider the impact of reflections and the physical dimensions of the accretion disk, the formula for determining the observed intensity on the screen is given by

$$\frac{d}{d\lambda} \left( \frac{I_\nu}{\nu^3} \right) = \frac{\mathcal{J}_\nu - \mathcal{K}_\nu I_\nu}{\nu^2}. \quad (48)$$

In this equation, the specific intensity is denoted as  $I_\nu$ , the emissivity as  $\mathcal{J}_\nu$ , and the absorption coefficient at frequency  $\nu$  as  $\mathcal{K}_\nu$ . In a vacuum, both  $\mathcal{J}_\nu$  and  $\mathcal{K}_\nu$  are zero, which implies that the specific intensity  $\frac{I_\nu}{\nu^3}$  is conserved along the geodesic path. In addition, the accretion disk exhibits a geometrically thin structure, and as light traverses it, both the absorption coefficient and emissivity of the accretion disk stay unchanged. Therefore, the light intensity detected on the screen can be expressed as

$$I_{\nu_o} = \sum_{n=1}^{N_{\text{max}}} \left( \frac{\nu_o}{\nu_n} \right)^3 \frac{\mathcal{J}_n}{\eta_{n-1}} \left[ \frac{1 - e^{\mathcal{K}_n f_n}}{\mathcal{K}_n} \right]. \quad (49)$$

Here,  $\nu_o$  is the observed frequency on the screen, which is  $\nu_o = \mathcal{E}_o = -p_0|_{r=r_o}$ , and  $\nu_n$  is the frequency observed by the local rest frames comoving with the accretion disk, where  $\nu_n = \mathcal{E}_n = -k_\mu u^\mu|_{r=r_n}$ . We denote  $f_n$  as the fudge factor that is related to the accretion disk model, and we can obtain  $f_n = \nu_n \Delta\lambda_n$ . When the ray traverses the accretion disk for the  $n^{\text{th}}$  time, its position is represented

by  $G_n$ , and the change in its affine parameter is denoted as  $\Delta\lambda_n$ . The required optical depth, denoted as  $\eta_m$ , is expressed as

$$\eta_m = \begin{cases} \exp \left[ \sum_{n=1}^m \mathcal{K}_n f_n \right], & \text{if } m \geq 1, \\ 1, & \text{if } m = 0. \end{cases} \quad (50)$$

In this study, we consider accretion disks that are both optically and geometrically thin; thus, the optical depth effect is negligible at 230 GHz. Furthermore, considering the redshift factor,  $g_n = \nu_o/\nu_n$ , Eq. (49) is rewritten as  $I_{\nu_o} = \sum_{n=1}^{N_{\text{max}}} f_n g_n^3 \mathcal{J}_n$ . In addition, combined with the EHT observations of M87\* and Sgr A\*, we can adopt the following emissivity prescription:

$$\mathcal{J} = \exp \left[ -\frac{1}{2} \left( \log \frac{r}{r_h} \right)^2 - 2 \log \frac{r}{r_h} \right], \quad (51)$$

The primary role of  $f_n$  is to modify the light intensity within the narrow photon ring, thus having minimal impact on the overall pattern. In this context,  $f_n$  is normalized to a value of 1. Note that the redshift factors  $g_n$  in the inner and outer regions of ISCO on the accretion disk also have different manifestations. When  $r \geq r_{\text{ISCO}}$

$$g_n = \frac{e}{\mathcal{P}(1 - \Omega_n \zeta)}, \quad (52)$$

whereas when  $r < r_{\text{ISCO}}$ , the value of the redshift factors is

$$g_n = -\frac{e}{u_{\text{in}}^r k_r / \vec{E} + \mathcal{E}_{\text{ISCO}}(g^{tt} - g^{t\phi}\zeta) + \mathcal{L}_{\text{ISCO}}(g^{\phi\phi}\zeta - g^{t\phi})}. \quad (53)$$

where  $\mathcal{P} = \sqrt{\frac{-1}{g_{tt} + 2g_{t\phi}\Omega_n + g_{\phi\phi}\Omega_n^2}}|_{r=r_n}$ . Moreover, in an asymptotically flat spacetime, when an observer is located infinitely far away, the relationship between the energy measured on the screen and the energy propagating along a null geodesic is given by  $e = \frac{\vec{E}_o}{\vec{E}}$ <sup>1)</sup>.

## B. Images of the rotation Loop Quantum Black Bounce

After characterizing the properties of the thin accretion disk model and quantifying the observable intensity received by the observer, we can simulate the image of the LQBB illuminated by the accretion disk on the observation plane. In comparison with the rotational direction of the LQBB, we examine two distinct types of accretion flow behavior: prograde and retrograde accretion flows. This consideration permits the presence of both forward and backward photons in the vicinity of the LQBB. In

1) Here, the value of  $e$  should be  $e=1$  [61] for a static observer at infinity in an asymptotically flat spacetime.



Fig. 4, we show the image of a rotating LQBB illuminated by prograde flows at different observation inclination angles  $\theta_{\text{obs}}$ , whereas the values of the other parameters are fixed as  $\alpha = 0.47$ ,  $a = 0.9$ , and  $r_{\text{obs}} = 100$ . In Fig. 5, the observation inclination angle is fixed as  $\theta_{\text{obs}} = 85^\circ$ , which shows the image of the rotating LQBB on the observation screen under different parameter spaces  $(\alpha, a)$ . The results demonstrate that, regardless of variations in the relevant parameters or observation angle, the observation plane consistently exhibits a dark region encircled by a brighter annular structure. The dark area represents the accretion disk image, often called the inner shadow. Meanwhile, the prominent luminous ring, referred to as the photon ring, aligns closely with the LQBB's critical curve. This indicates that these characteristics are intrinsic spacetime properties of the LQBB.

At a lower observation angle, such as  $\theta_{\text{obs}} = 20^\circ$ , the inner shadow remains a nearly circular black disk, but the photon ring is no longer centrosymmetric with the inner shadow. However, owing to the relatively uniform and concentrated distribution of light intensity around the inner shadow, we cannot directly differentiate between the direct and lensed images of the accretion disk. As the observed inclination continues to increase, the deformation of the inner shadow can be clearly identified. When  $\theta_{\text{obs}} = 40^\circ$ , the inner shadow begins to deform slightly. When the observed inclination angle reaches a significant value, such as  $\theta_{\text{obs}} = 85^\circ$ , the deformation of the inner shadow becomes extremely pronounced, adopting a D-shape appearance. At this point, the luminosity surrounding the inner shadow begins to converge towards the top of the screen, with a conspicuous bright arc forming on the left side of the display. The reason for this phenomenon is that the accretion flow moves in the same direction as the black hole's rotation. Owing to the Doppler effect, the side of the accretion flow moving towards the observer appears to accumulate more energy. Thus, at a larger observation angle, the direct and lensed images of the accretion disk gradually separate, forming a hat-like morphology.

In Fig. 5, from left to right columns, the value of  $\alpha$  is fixed, and  $a$  is set to 0.1, 0.4, 0.7, and 0.9, respectively, to

demonstrate the impact of  $a$  on the LQBB observation image. From the top row to the bottom row, the graphs illustrate the influence of varying  $\alpha$  on the image characteristics. By comparing the shadow outline of LQBB, the inner shadows at  $\theta_{\text{obs}} = 85^\circ$  all exhibit significant deformations, appearing as a smooth small semi-circular black area. Specifically, when  $\alpha$  is held constant and  $a$  increases, the inner shadow area contracts, and luminosity converges toward the upper portion of the screen. For the same  $a$ , as  $\alpha$  increases, the size of the inner shadow area shrinks slightly, which is weaker than the effect of  $a$ . In addition, as  $a$  gradually increases, both the overall observed light intensity of the image and  $\alpha$  exhibit an upward trend.

For retrograde accretion flow, Fig. 6 presents the image of the LQBB. Furthermore, to facilitate a more accurate comparison of shadow images under the two accretion modes, we have generated corresponding shadow images using the same set of parameters, specifically referencing the parameter values listed in the last row of Fig. 5. Fig. 6 also shows that the inner shadow and critical curve decrease as  $a$  increases, similar to the behavior under prograde flows. However, regarding the intensity distribution, prograde and retrograde accretion disks exhibit distinct behaviors. For prograde flows, the light intensity observed on the left side of the critical curve is significantly stronger than that on the right side. In contrast, for the countercurrent, the observed light intensity is significantly stronger on the right than on the left, with a large amount of observed light intensity concentrated on the upper right side of the screen. Similarly, a retrograde accretion disk rotates to the right, accumulating strength on the right side. Additionally, the strength of retrograde flow is somewhat lower than that of prograde flow, which is consistent with the previous results.

To emphasize the lensing band features of the accretion disk, we illustrate the non-uniform resolution used for image computation and storage across various parameter values. In these figures, each band is designed to contain approximately the same number of pixels, which simplifies the management of pixel counts per image. In the rotating LQBB spacetime, three distinct regions ap-

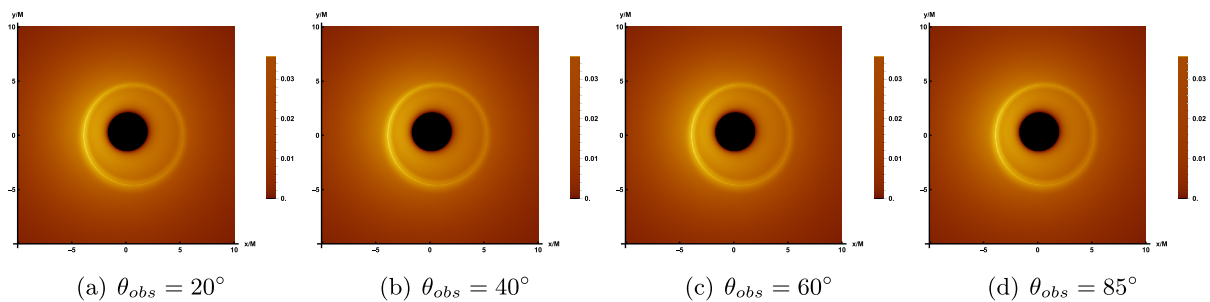
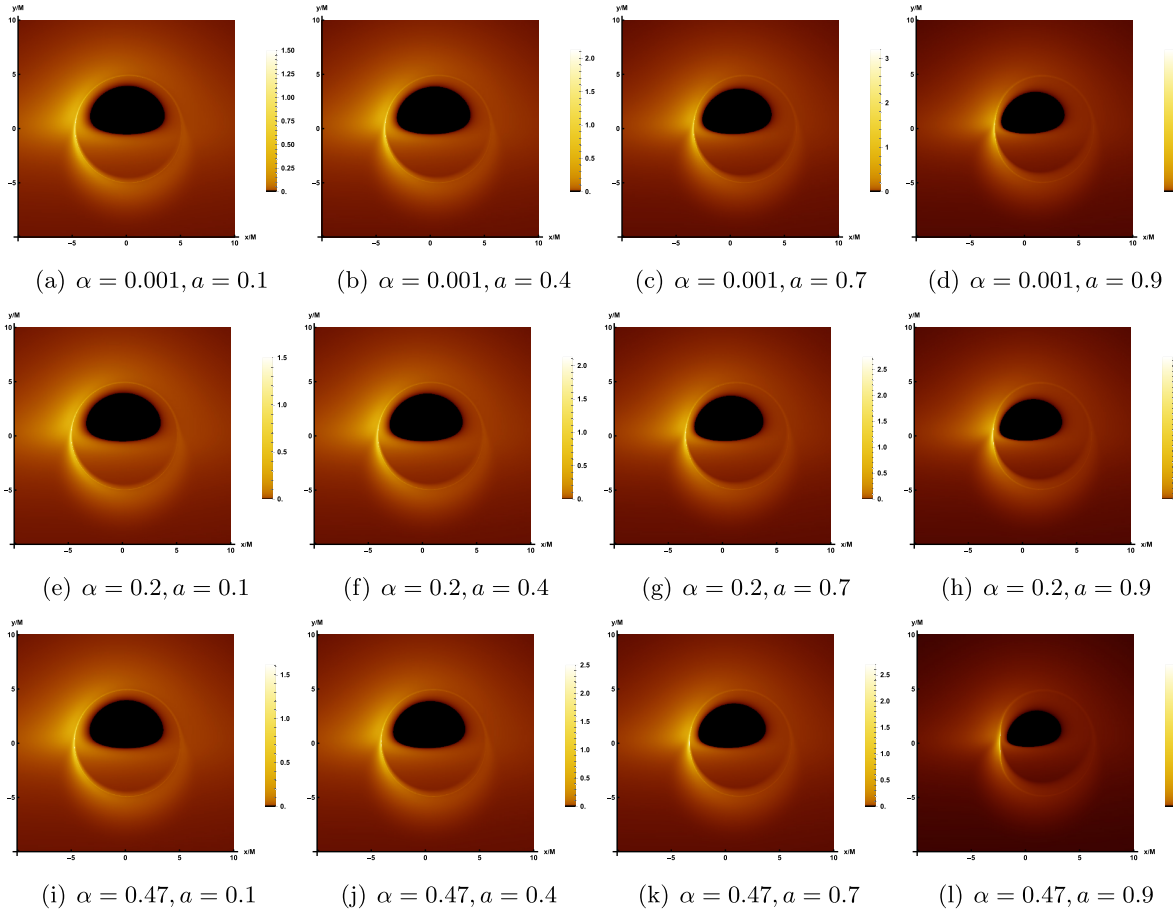
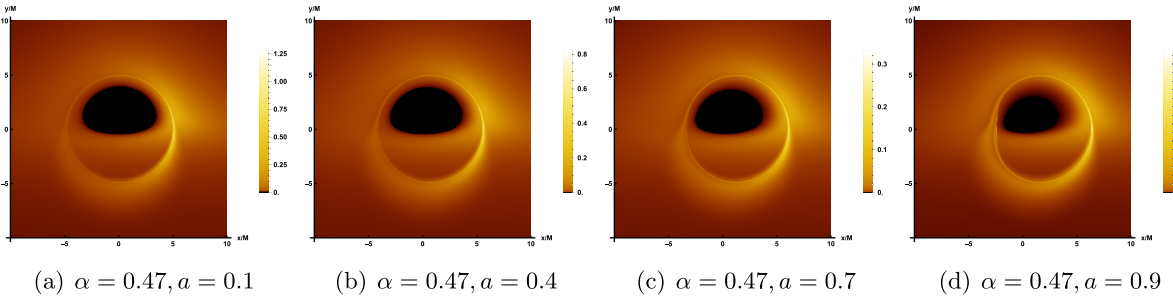


Fig. 4. (color online) Image of the LQBB surrounded by prograde flow at 230 GHz, where the relevant parameters are taken as  $\alpha = 0.47$ ,  $r_{\text{obs}} = 100$ , and  $a = 0.9$ . From the left to the right panel, the observed inclination  $\theta_{\text{obs}}$  increases gradually.



**Fig. 5.** (color online) Image of the rotating LQBB illuminated by prograde flows at 230 GHz, where the observed inclination is taken as  $\theta_{\text{obs}} = 85^\circ$  and  $r_{\text{obs}} = 100$ .



**Fig. 6.** (color online) Image of the rotating LQBB illuminated by retrograde flows at 230 GHz, where the observed inclination is taken as  $\theta_{\text{obs}} = 85^\circ$  and  $r_{\text{obs}} = 100$ .

pear, shown in green, red, and blue, corresponding to light that intersects the black hole's equatorial plane once, twice, and three times or more, respectively. That is, green, red, and blue represent the direct radiation region, lens radiation region, and critical curve, respectively. In addition, the innermost black region corresponds to the inner shadow of an LQBB.

Figure 7 depicts the lensing bands of the LQBB at different observation inclination angles, where the values of parameters correspond to those in Fig. 4. Upon com-

parison, we observe that, as the observation inclination angle increases, the lensed band gradually extends toward the lower left side of the screen. At a smaller angle, the lens band can maintain an approximately circular ring structure. However, at a larger angle, the lens band undergoes significant deformation and elongation, resulting in a significant increase in its proportion of the screen area. In Fig. 8, the top row illustrates the impact of varying  $a$  on the lensing bands, whereas the bottom row demonstrates the effect of altering  $\alpha$  on the lensing bands, with

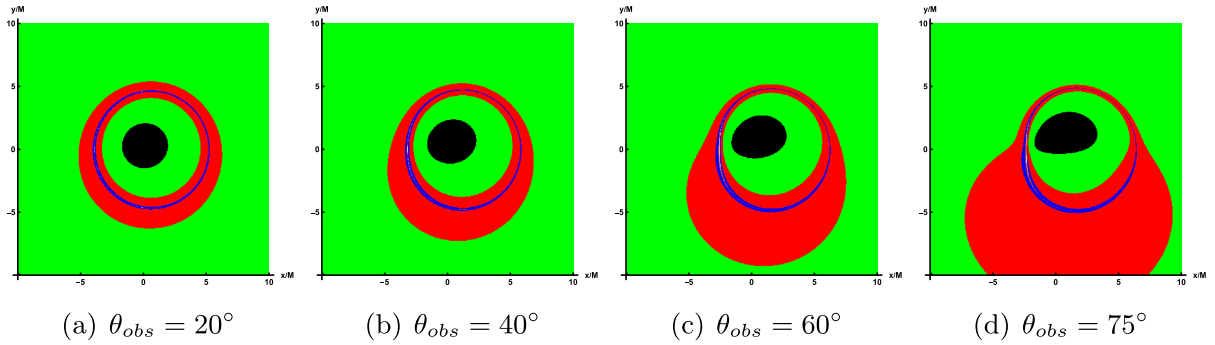
the observed inclination fixed at  $\theta_{\text{obs}} = 75^\circ$ . In all these cases, the critical curve always lie exactly within the red and green lensing bands. Subsequently, the increase in the rotation parameter significantly reduces the size of the critical curve, although increasing  $\alpha$  also has the same effect, and it is far less apparent than that of  $a$ .

### C. Distribution of redshifts

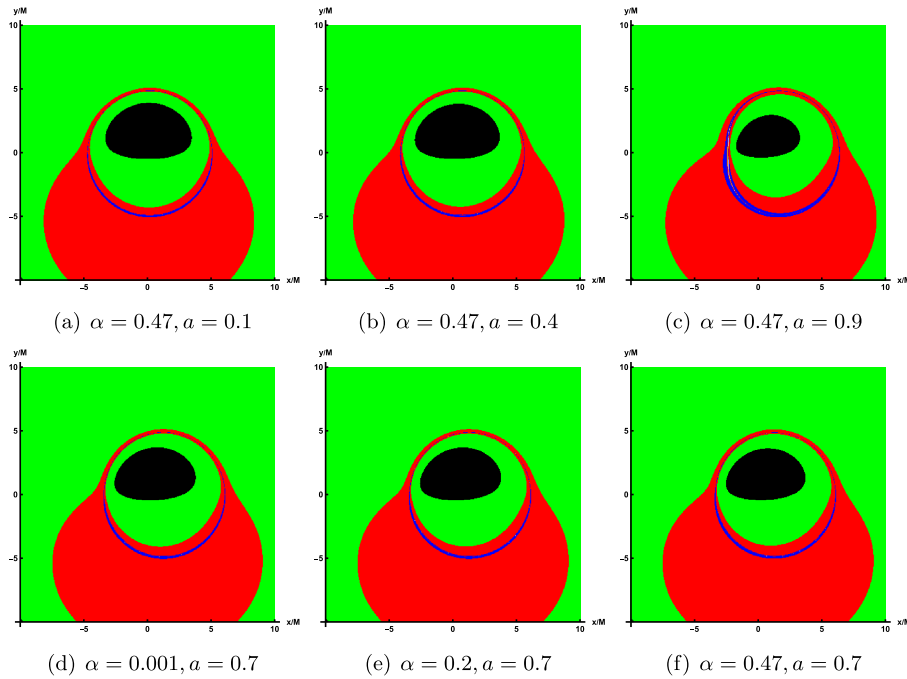
Considering the relative movement between the accretion flow and the observer, we should consider the impact of the Doppler effect during the imaging process. Consequently, when generating images of a black hole, we must examine the redshift factor associated with the dynamics of the emitted particles.

Figure 9 shows the redshift distribution of the direct image (top row) and lensed image (bottom row) of the

prograde accretion disk at different observation angles  $\theta_{\text{obs}}$ . Among them, the values of relevant parameters correspond to Fig. 4, and the observation angle changes to  $20^\circ$ ,  $40^\circ$ ,  $60^\circ$ ,  $75^\circ$ . From the top row of Fig. 9, the results show that, at a small observation angle  $\theta_{\text{obs}} = 20^\circ$ , only the redshift factor is distributed around the inner shadow region of the image and is relatively evenly distributed across the entire screen. As the observation angles increases to  $\theta_{\text{obs}} = 40^\circ$ , a smaller portion of the blueshift appears on the left side of the screen, and the redshift begins to concentrate to the right. As the observation angle continuously increases, the blueshift distribution observed on the screen increases steadily. When  $\theta_{\text{obs}} = 75^\circ$ , pronounced blueshift characteristics are evident on the left side of the screen, whereas redshift phenomena are predominantly concentrated on the right side, displaying



**Fig. 7.** (color online) Lensing bands of the LQBB for prograde accretion flow under different observation angles. Here, the representative parameters are set as  $\alpha = 0.47$  and  $a = 0.9$ . The observation angles, from left to right, are  $\theta_{\text{obs}} = 20^\circ$ ,  $40^\circ$ ,  $60^\circ$ ,  $75^\circ$ .



**Fig. 8.** (color online) Lensing bands of the LQBB for prograde accretion flow under various representative parameters ( $\alpha$ ,  $a$ ), with the observation angle fixed at  $\theta_{\text{obs}} = 75^\circ$ .

a notable contracting trend. In the bottom row of Fig. 9, the effect of varying the observation inclination on the lensed image shows similarities to that observed in direct images. A blueshift is only noticeable at higher observation inclinations, predominantly in the lower left quadrant of the screen. This phenomenon occupies a limited region, forming an eyebrow-like shape.

Subsequently, the effect of changes in the relevant parameters ( $\alpha, a$ ) on the redshift distribution in the direct image is shown in Fig. 10, where the values of the parameters correspond to Fig. 2 and the observed inclination is fixed at  $\theta_{\text{obs}} = 75^\circ$ . Overall, when  $a$  increases, the inner shadow decreases; therefore, the region of redshift appears to be smaller, whereas an increase in  $\alpha$  enhances the region of redshift. For the redshift of lensed images, shown in Fig. 11, the results are similar to those of the direct images.

Now, we describe the redshift distribution details of the retrograde accretion disk observed on the observer's screen; see Fig. 12. The parameter values in Fig. 12 are also consistent with the bottom line in Fig. 10. Based on Fig. 12, we observe that the inner shadow of the black hole remains constant under identical parameters. Nevertheless, when compared with the prograde case, the regions of redshift and blueshift are inverted, and the area of redshift surrounding the shadow exhibits a slight expansion. Furthermore, the position of maximum light intensity on the screen has shifted to the right side of the shadow, as opposed to being on the left side as observed in the prograde scenario. The impact of  $a$  on the shadow, redshift, and light intensity corresponds with the observations in the prograde case.

## VI. CONCLUSION AND DISCUSSION

The shadow of a black hole is a fascinating phenomenon surrounding this enigmatic object, essentially serving as its cosmic silhouette. This shadow occurs due to the extreme bending of spacetime caused by the black hole's immense gravitational pull, as predicted by Einstein's general theory of relativity. When light rays traverse the curved spacetime near a black hole, they are deflected, and any light crossing the event horizon is trapped, unable to escape. Consequently, a dark void forms around the black hole, known as its shadow. The study of black hole shadows is pivotal for understanding the properties of black holes and testing the boundaries of general relativity. The historic first image of a black hole's shadow provided direct visual evidence of this phenomenon, revealing an asymmetric ring structure around the darkness, shaped by strong gravitational lensing and relativistic beaming effects. The shape, size, and luminosity of the shadow, along with the surrounding emissions, offer invaluable insights into the accretion processes and radiation mechanisms near black holes. They also reflect the nature of spacetime around these celestial bodies, serving as a potential tool to scrutinize various gravitational theories.

By considering a zero-angular-momentum observer, we employ the backward ray-tracing method to investigate the shadows and images of the accretion disk of a rotation LQBB. Our findings reveal that the the contour size of the shadow expands as the rotation parameter  $a$  increases, as illustrated in Fig. 1. Furthermore, when  $a$  and the observation inclination  $\theta_{\text{obs}}$  are larger, although the contour of the shadow is deformed to the limiting D-shape, the increase in the LQG parameter  $\alpha$  will still

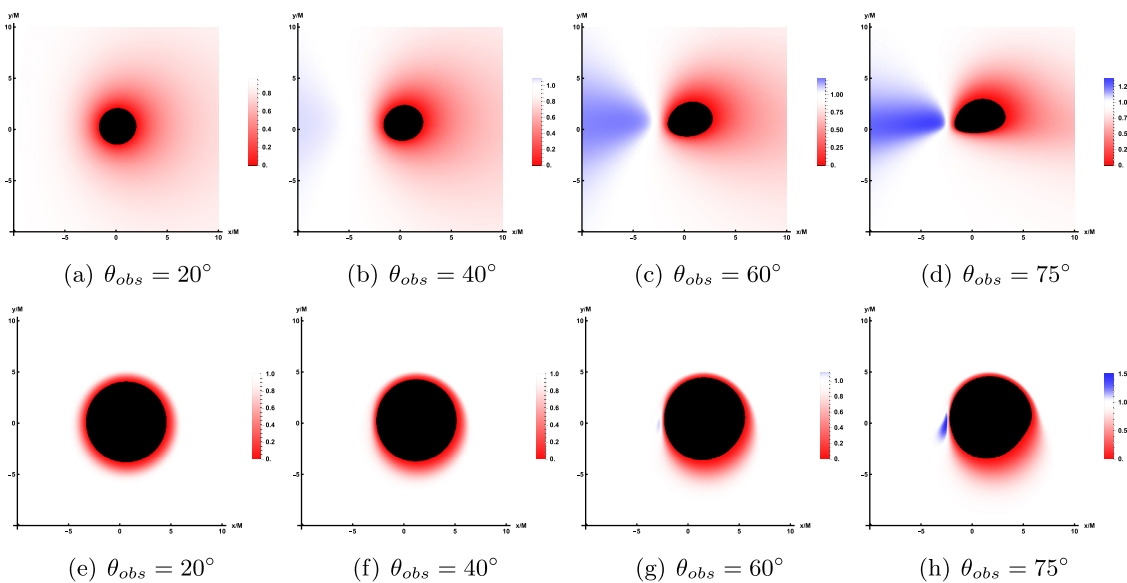


**Fig. 9.** (color online) Redshift distribution of the direct image (bottom row) and lensed image (bottom row) under prograde accretion flow. Here, the correlation parameter is set to  $\alpha = 0.47$  and  $a = 0.9$ , whereas the observation angles are  $\theta_{\text{obs}} = 20^\circ, 40^\circ, 60^\circ$  and  $75^\circ$ .

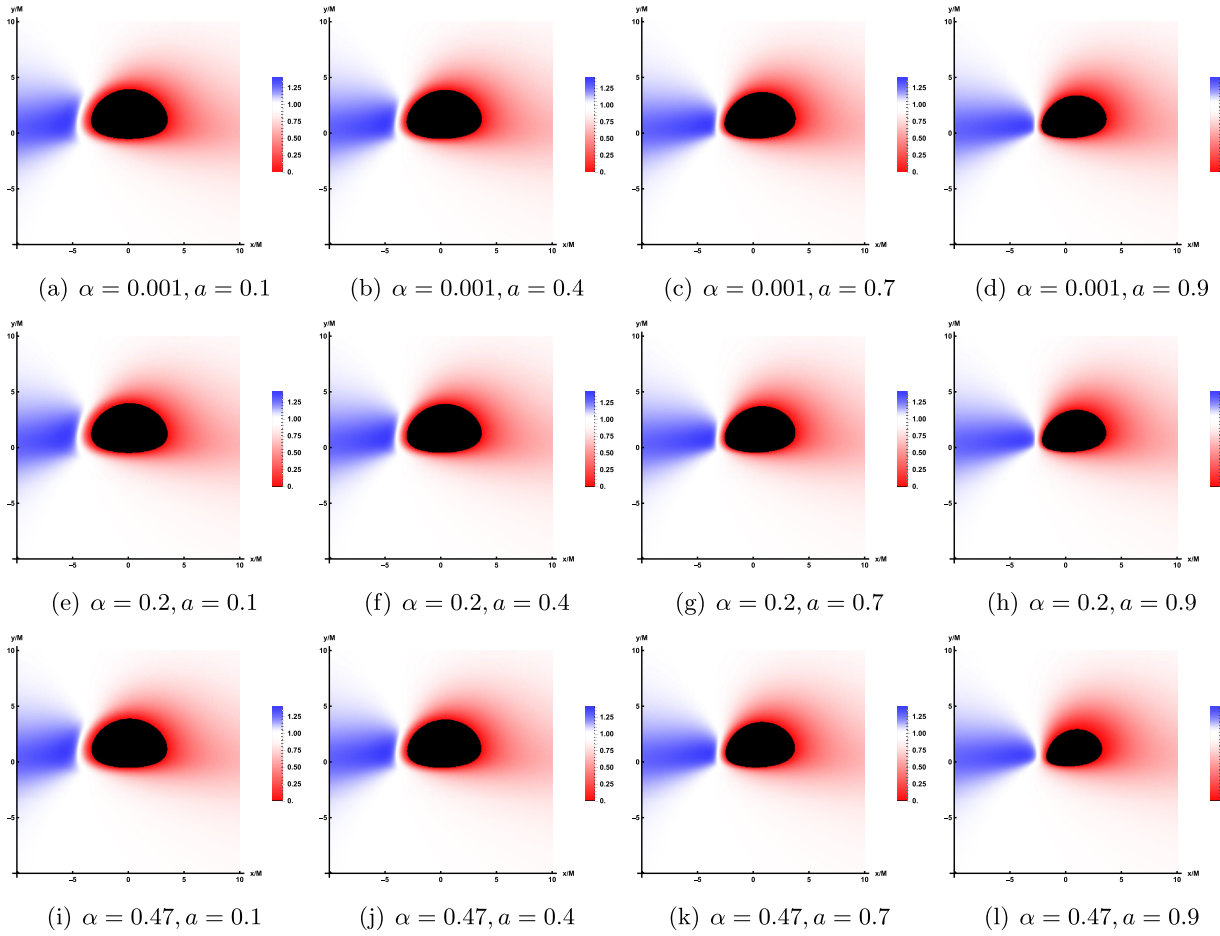


**Fig. 10.** (color online) Redshift distribution of the direct image under prograde accretion flow, where the observation angle is  $\theta_{\text{obs}} = 75^\circ$ . Here, the value of  $a$  increases from left to right while the value of  $\alpha$  remains unchanged, and the value of  $\alpha$  increases from top to bottom while the value of parameter  $a$  remains unchanged.

cause the shadow to shrink on the horizontal axis. To visualize the effect of a strong gravitational field on light around a black hole, we also study images of black holes illuminated by astrophysical light sources. As  $a$  increases, the D-shape shadow induced by a diminishes. At a wide field of view, the shadow area on the screen is encircled by an axisymmetric ring, known as the Einstein ring. Notably, the shape of this ring remains unaffected by variations in the rotation parameter.

To explore the optical characteristics of the rotation LQBB, we expand the accretion disk model to a scenario in which the innermost part of the accretion disk reaches the event horizon of the black hole. In this scenario, the redshift distribution and radiation characteristics within the ISCO must be reassessed, given the different particle motion behaviors inside and outside the ISCO, along with performing more comprehensive ray-tracing computations across a wider integration area. Meanwhile, with respect to the direction of rotation of the black hole, two cases of accretion flow behavior are considered: prograde and retrograde accretion flows. The results show

that, at a large  $\theta_{\text{obs}}$ , we can easily distinguish between direct and lensed images, but at a small  $\theta_{\text{obs}}$ , they become difficult to distinguish. As the observation angle continuously increases, the observation intensity of the image gradually focuses on the left side of the screen for prograde accretion flow, whereas the observation intensity of the image focuses on the right side of the screen for retrograde accretion flow. This is attributed to the Doppler effect, as the prograde accretion disk rotates to the left, leading to an accumulation of intensity on the left. Conversely, in a retrograde disk rotating to the right, the intensity accumulates on the right side. In addition, an increase in  $a$  enhances the observation intensity, as well as  $\alpha$ .

Subsequently, we study the redshift distribution of both the direct and lensed images from the accretion disk. For prograde accretion flow, only the redshift is observed on the screen for a small observation angle. Conversely, at larger observation angles, the redshift is primarily observed on the right side of the screen, whereas a blueshift begins to emerge on the left side. An in-



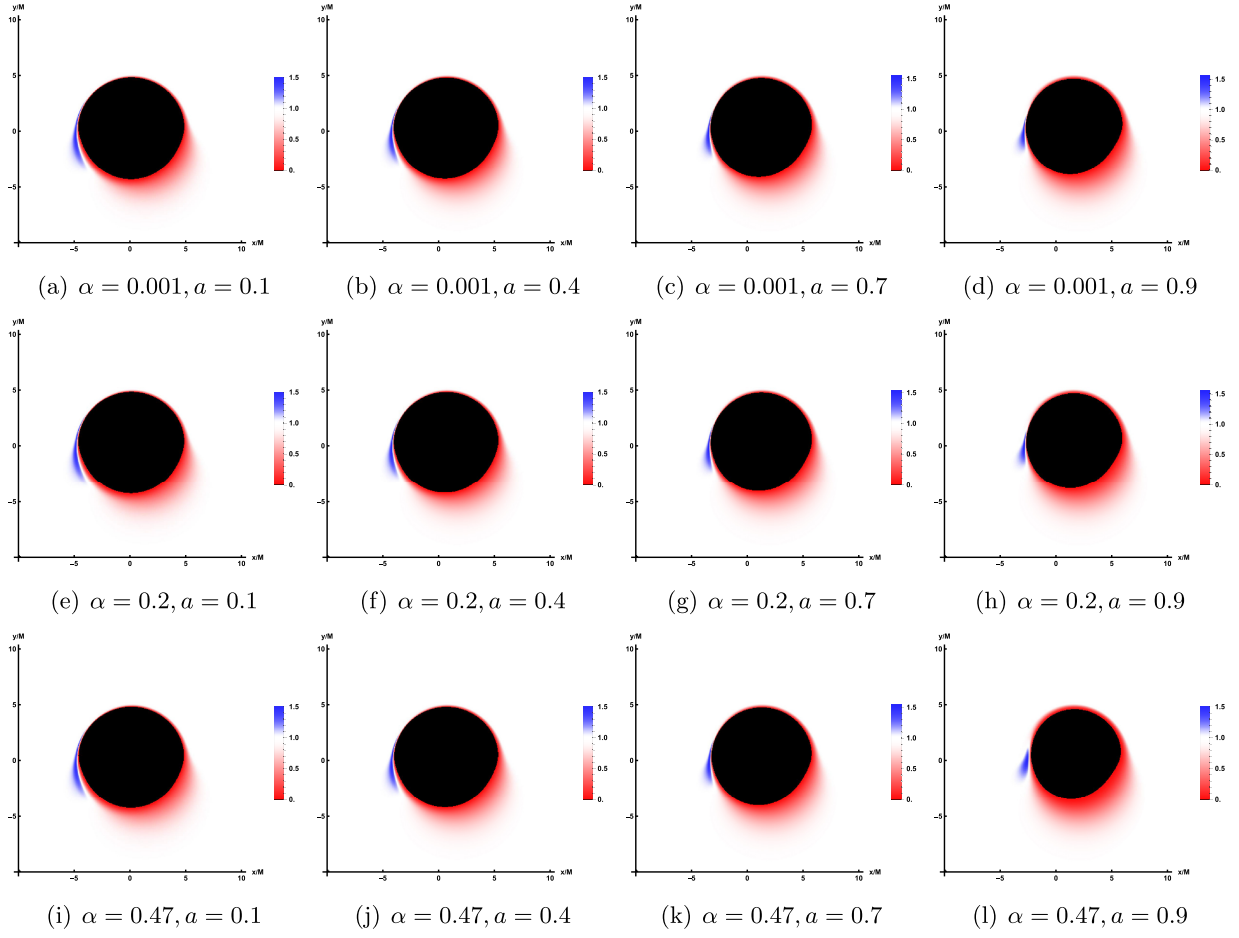


**Fig. 11.** (color online) Redshift distribution of the lensed image under prograde accretion flow, where the observation angles is  $\theta_{\text{obs}} = 75^\circ$ . The values of related parameters are consistent with those of the direct image.

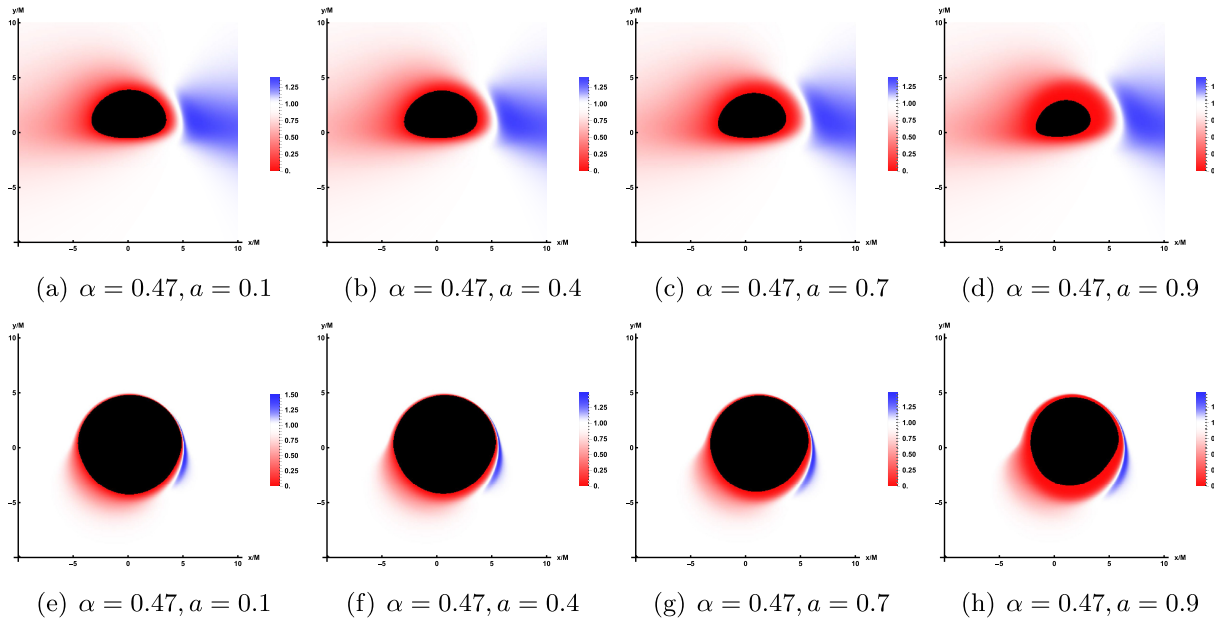


**Fig. 12.** (color online) Redshift distribution of the direct image (bottom row) and lensed image (top row) under retrograde accretion flow. Here, the correlation parameter is set to  $\alpha = 0.47$  and  $\theta_{\text{obs}} = 75^\circ$ , whereas the rotation parameters are  $a = 0.1, 0.4, 0.7$ , and  $0.9$ .

crease in  $a$  and  $\alpha$  decreases the blueshift. For retrograde accretion flow, the influence of the relevant parameters on the redshift and blueshift is analogous to that observed in prograde accretion flow. However, the distributions of the redshift and blueshift are exactly reversed with respect to the results of the prograde case. In summary,  $a$  has significant impacts on the image of the rota-

tion LQBB. Although  $\alpha$  does not affect the observed appearance of the black hole as much as  $a$  does, it has a catalytic effect. The influence of  $\alpha$  on the black hole image, including its shadow and light intensity, can serve as an effective method for differentiating these black holes from the Kerr black hole. This distinction may offer valuable insights for astronomical observations.

## References

- [1] K. Akiyama *et al.* (Event Horizon Telescope Collaboration), *Astrophys. J. Lett.* **875**, L1 (2019)
- [2] K. Akiyama *et al.* (Event Horizon Telescope Collaboration), *Astrophys. J. Lett.* **875**(1), L2 (2019)
- [3] K. Akiyama *et al.* (Event Horizon Telescope Collaboration), *Astrophys. J. Lett.* **875**(1), L3 (2019)
- [4] K. Akiyama *et al.* (Event Horizon Telescope Collaboration), *Astrophys. J. Lett.* **875**(1), L4 (2019)
- [5] K. Akiyama *et al.* (Event Horizon Telescope Collaboration), *Astrophys. J. Lett.* **875**(1), L5 (2019)
- [6] K. Akiyama *et al.* (Event Horizon Telescope Collaboration), *Astrophys. J. Lett.* **875**(1), L6 (2019)
- [7] K. Akiyama *et al.* (Event Horizon Telescope Collaboration), *Astrophys. J. Lett.* **930**(2), L12 (2022)
- [8] K. Akiyama *et al.* (Event Horizon Telescope Collaboration), *Astrophys. J. Lett.* **930**(2), L13 (2022)
- [9] K. Akiyama *et al.* (Event Horizon Telescope Collaboration), *Astrophys. J. Lett.* **930**(2), L14 (2022)
- [10] K. Akiyama *et al.* (Event Horizon Telescope Collaboration), *Astrophys. J. Lett.* **930**(2), L15 (2022)
- [11] K. Akiyama *et al.* (Event Horizon Telescope Collaboration), *Astrophys. J. Lett.* **930**(2), L16 (2022)
- [12] K. Akiyama *et al.* (Event Horizon Telescope Collaboration), *Astrophys. J. Lett.* **930**(2), L17 (2022)
- [13] J. L. Synge, *Mon. Not. Roy. Astron. Soc.* **131**(3), 463 (1966)
- [14] J.M. Bardeen, Proceedings, Ecole d'Eté de, *Physique Théorique: Les Astres Occlus: Les Houches*, (France, 1973) pp. 215
- [15] S. Chandrasekhar, *The Mathematical Theory of Black Holes*, (New York: Oxford University Press, 1992)
- [16] S. W. Wei and Y. X. Liu, *JCAP* **11**, 063 (2013)
- [17] S. W. Wei, P. Cheng, Y. Zhong *et al.*, *JCAP* **08**, 004 (2015)
- [18] Y. Huang, S. Chen, and J. Jing, *Eur. Phys. J. C* **76**(11), 594 (2016)
- [19] M. Wang, S. Chen, and J. Jing, *JCAP* **10**, 051 (2017)
- [20] K. J. He, J. T. Yao, X. Zhang *et al.*, *Phys. Rev. D* **109**(6), 064049 (2024)
- [21] M. Wang, G. Guo, P. Yan *et al.*, *Chin. Phys. C* **48**(10), 105103 (2024)
- [22] M. Guo and P. C. Li, *Eur. Phys. J. C* **80**(6), 588 (2020)
- [23] F. Atamurotov, A. Abdujabbarov, and B. Ahmedov, *Phys. Rev. D* **88**(6), 064004 (2013)
- [24] V. Perlick, O. Y. Tsupko, and G. S. Bisnovatyi-Kogan, *Phys. Rev. D* **92**(10), 104031 (2015)
- [25] R. A. Konoplya, *Phys. Lett. B* **795**, 1 (2019)
- [26] R. Shaikh, P. Kocherlakota, R. Narayan *et al.*, *Mon. Not. Roy. Astron. Soc.* **482**(1), 52 (2019)
- [27] A. Abdujabbarov, M. Amir, B. Ahmedov *et al.*, *Phys. Rev. D* **93**(10), 104004 (2016)
- [28] L. Amarilla and E. F. Eiroa, *Phys. Rev. D* **85**, 064019 (2012)
- [29] P. G. Nedkova, V. K. Tinchev, and S. S. Yazadjiev, *Phys. Rev. D* **88**(12), 124019 (2013)
- [30] U. Papnoi, F. Atamurotov, S. G. Ghosh *et al.*, *Phys. Rev. D* **90**(2), 024073 (2014)
- [31] Y. Meng, X. M. Kuang, X. J. Wang *et al.*, *Phys. Lett. B* **841**, 137940 (2023)
- [32] Z. Zhang, Y. Hou, and M. Guo, *Chin. Phys. C* **48**(8), 085106 (2024)
- [33] Z. Zhang, H. Yan, M. Guo *et al.*, *Phys. Rev. D* **107**(2), 024027 (2023)
- [34] K. Hashimoto, S. Kinoshita, and K. Murata, *Phys. Rev. Lett.* **123**(3), 031602 (2019)
- [35] K. Hashimoto, S. Kinoshita, and K. Murata, *Phys. Rev. D* **101**(6), 066018 (2020)
- [36] X. X. Zeng, L. F. Li, P. Li *et al.*, *Sci. China Phys. Mech. Astron.* **68**(2), 220412 (2025)
- [37] X. X. Zeng, K. J. He, J. Pu *et al.*, *Eur. Phys. J. C* **83**(10), 897 (2023)
- [38] Y. Liu, Q. Chen, X. X. Zeng *et al.*, *JHEP* **10**, 189 (2022)
- [39] K. J. He, Y. W. Han, and G. P. Li, *Nucl. Phys. B* **1010**, 116768 (2025)
- [40] K. J. He, Y. W. Han, and G. P. Li, *Phys. Dark Univ.* **44**, 101468 (2024)
- [41] R. Narayan, M. D. Johnson, and C. F. Gammie, *Astrophys. J. Lett.* **885**(2), L33 (2019)
- [42] S. E. Gralla, D. E. Holz, and R. M. Wald, *Phys. Rev. D* **100**(2), 024018 (2019)
- [43] R. A. Konoplya and A. Zhidenko, *Phys. Rev. D* **103**(10), 104033 (2021)
- [44] A. Chowdhuri and A. Bhattacharyya, *Phys. Rev. D* **104**(6), 064039 (2021)
- [45] N. Tsukamoto, Z. Li, and C. Bambi, *JCAP* **06**, 043 (2014)
- [46] P. V. P. Cunha, C. A. R. Herdeiro, E. Radu *et al.*, *Phys. Rev. Lett.* **115**(21), 211102 (2015)
- [47] S. Chen, J. Jing, W. L. Qian *et al.*, *Sci. China Phys. Mech. Astron.* **66**(6), 260401 (2023)
- [48] K. J. He, Z. Luo, S. Guo *et al.*, *Chin. Phys. C* **48**(6), 065105 (2024)
- [49] X. X. Zeng, G. P. Li, and K. J. He, *Nucl. Phys. B* **974**, 115639 (2022)
- [50] K. J. He, S. C. Tan, and G. P. Li, *Eur. Phys. J. C* **82**(1), 81 (2022)
- [51] K. J. He, X. Zhang, and X. Li, *Chin. Phys. C* **46**(7), 075103 (2022)
- [52] G. P. Li and K. J. He, *Eur. Phys. J. C* **81**(11), 1018 (2021)
- [53] X. X. Zeng, K. J. He, and G. P. Li, *Sci. China Phys. Mech. Astron.* **65**(9), 290411 (2022)
- [54] Z. Zhang, S. Chen, and J. Jing, *JCAP* **09**, 027 (2024)
- [55] H. M. Wang, Z. C. Lin, and S. W. Wei, *Nucl. Phys. B* **985**, 116026 (2022)

- [56] Q. Gan, P. Wang, H. Wu *et al.*, *Phys. Rev. D* **104**(4), 044049 (2021)
- [57] G. P. Li, H. B. Zheng, K. J. He *et al.*, *Eur. Phys. J. C* **85**(3), 249 (2025)
- [58] G. P. Li, M. Q. Wu, K. J. He *et al.*, arXiv: 2505.14734[gr-qc]
- [59] G. P. Li and K. J. He, *JCAP* **06**, 037 (2021)
- [60] G. P. Li, K. J. He, X. Y. Hu *et al.*, *Front. Phys. (Beijing)* **19**(5), 54202 (2024)
- [61] Y. Hou, Z. Zhang, H. Yan *et al.*, *Phys. Rev. D* **106**(6), 064058 (2022)
- [62] C. Y. Yang, M. I. Aslam, X. X. Zeng *et al.*, arXiv: 2411.11807[astro-ph.HE]
- [63] S. Guo, Y. X. Huang, E. W. Liang *et al.*, *Astrophys. J.* **975**(2), 237 (2024)
- [64] K. J. He, G. P. Li, C. Y. Yang *et al.*, *Eur. Phys. J. C* **85**(6), 662 (2025)
- [65] K. J. He, C. Y. Yang, and X. X. Zeng, arXiv: 2501.06778[astro-ph.HE]
- [66] Y. Meng, X. J. Wang, Y. Z. Li *et al.*, arXiv: 2501.02496[gr-qc]
- [67] C. Rovelli, *Living Rev. Rel.* **1**, 1 (1998)
- [68] K. A. Meissner, *Class. Quant. Grav.* **21**, 5245 (2004)
- [69] M. Han, W. Huang, and Y. Ma, *Int. J. Mod. Phys. D* **16**, 1397 (2007)
- [70] J. Yang, Y. Ding, and Y. Ma, *Phys. Lett. B* **682**, 1 (2009)
- [71] X. Zhang and Y. Ma, *Phys. Rev. Lett.* **106**, 171301 (2011)
- [72] Y. Ma, C. Soo, and J. Yang, *Phys. Rev. D* **81**, 124026 (2010)
- [73] A. Ashtekar, T. Pawłowski, P. Singh *et al.*, *Phys. Rev. D* **75**, 024035 (2007)
- [74] K. Vandersloot, *Phys. Rev. D* **75**, 023523 (2007)
- [75] M. Bojowald, *Phys. Rev. Lett.* **86**, 5227 (2001)
- [76] M. Bojowald, *Class. Quant. Grav.* **19**, 2717 (2002)
- [77] A. Ashtekar, M. Bojowald, and J. Lewandowski, *Adv. Theor. Math. Phys.* **7**(2), 233 (2003)
- [78] A. Ashtekar, T. Pawłowski, and P. Singh, *Phys. Rev. D* **74**, 084003 (2006)
- [79] A. Ashtekar, J. Olmedo, and P. Singh, arXiv: 2301.01309[gr-qc]
- [80] L. Modesto, *Int. J. Theor. Phys.* **45**, 2235 (2006)
- [81] A. Ashtekar and M. Bojowald, *Class. Quant. Grav.* **23**, 391 (2006)
- [82] L. Modesto, *Class. Quant. Grav.* **23**, 5587 (2006)
- [83] G. Ongole, P. Singh, and A. Wang, *Phys. Rev. D* **109**(2), 026015 (2024)
- [84] A. Perez, *Living Rev. Rel.* **16**, 3 (2013)
- [85] J. Engle and S. Speziale, arXiv: 2310.20147[gr-qc]
- [86] C. Rovelli and F. Vidotto, *Cambridge Monographs on Mathematical Physics*, (Cambridge University Press, 2014)
- [87] C. R. Muniz, G. Alencar, M. S. Cunha *et al.*, arXiv: 2408.08542[gr-qc]
- [88] J. G. Kelly, R. Santacruz, and E. Wilson-Ewing, *Phys. Rev. D* **102**(10), 106024 (2020)
- [89] J. Lewandowski, Y. Ma, J. Yang *et al.*, *Phys. Rev. Lett.* **130**(10), 101501 (2023)
- [90] A. Simpson and M. Visser, *JCAP* **02**, 042 (2019)
- [91] M. Azreg-Aïnou, *Phys. Rev. D* **90**(6), 064041 (2014)
- [92] M. Azreg-Aïnou, *Phys. Lett. B* **730**, 95 (2014)
- [93] S. Brahma, C. Y. Chen, and D. h. Yeom, *Phys. Rev. Lett.* **126**(18), 181301 (2021)
- [94] C. Y. Chen, *Int. J. Geom. Meth. Mod. Phys.* **19**(11), 2250176 (2022)
- [95] Z. Hu, Z. Zhong, P. C. Li *et al.*, *Phys. Rev. D* **103**(4), 044057 (2021)
- [96] A. Chael, M. D. Johnson, and A. Lupasca, *Astrophys. J.* **918**(1), 6 (2021)